Transportation Geotechnics 57 (2026) 101879

Contents lists available at ScienceDirect

Transportation Geotechnics

journal homepage: www.elsevier.com/locate/trgeo

Multi-objective Optimization of Railway Transition Zones with Machine Learning: Application to Prefabricated Epoxy Asphalt Cured Track Bed

You Wu [a], Chenguang Shi [b,*], Yunhong Yu [c], Yulou Fan [c], Jun Yang [c]

[a] Section of Railway Engineering, Delft University of Technology, Stevinweg 1, 2628 CN Delft, the Netherlands
[b] National & Local Joint Engineering Research Center of Transportation Civil Engineering Materials, Chongqing Jiaotong University, Chongqing 400074, China
[c] School of Transportation, Southeast University, #2 Southeast University Road, Nanjing 211189, China

ARTICLE INFO

Keywords:
High-speed railway
Transition zone
Epoxy asphalt cured trackbed
Finite element modeling
Machine learning
Multi-objective optimization

ABSTRACT

Transition zones in high-speed railways suffer from abrupt stiffness variations that induce irregular dynamic responses and accelerate infrastructure deterioration. This study presents a surrogate-assisted multi-objective optimization framework that combines finite element (FE) simulations, a neural network-based surrogate model, and the NSGA-II algorithm to address this challenge. A validated 3D FE model of prefabricated epoxy asphalt cured track beds (PEACT) was used to generate 341 layout scenarios covering 13 response parameters. These data were used to train a neural network, which served as a static surrogate predictor for evaluating layout performance during the optimization process. The results show that module layout has a limited effect on peak responses but significantly improves smoothness, with three categories of optimal configurations identified. Compared with direct FE-based optimization, the proposed framework achieves substantial computational efficiency and provides data-driven design guidance for PEACT transition zones. This framework exemplifies the potential of hybrid data–simulation approaches to enhance adaptive and efficient railway infrastructure design.

Introduction

The rapid development of high-speed railway (HSR) worldwide has revolutionized modern transportation, enabling faster, more efficient, and more comfortable travel over long distances. However, as train speeds increase, the dynamic interaction between vehicles and track structures becomes significantly sensitive to local discontinuities, especially vertical stiffness variations in the longitudinal direction [1–3]. One critical section is the transition zones, which occur while the track support changes, either between different types of track structures, such as between ballasted track and bridges [4], tunnels [5], or slab tracks [6], or even within the same type of track when laid on different substructures. In HSR lines, these transition zones are particularly vulnerable to stiffness mismatches, which can cause abrupt changes in structural responses as trains pass through.

With the increasing use of longer bridges, extended slab tracks, and higher train speeds, the importance of effective transition zone design has become more pronounced. In response, various transition structures have been developed to accommodate changes in track stiffness, including the use of new materials [7,8] and innovative structure configurations [4]. Solutions such as elastic layers or damping materials, including geogrids [9] and polyurethane [10], have demonstrated benefits in reducing stiffness discontinuities. Meanwhile, structural approaches like graded sleeper spacing [11], variable ballast thickness [12], and under-sleeper pads [13] offer further performance improvements. However, these measures are often optimized for specific design conditions and may face challenges in adapting to evolving operational requirements or diverse site environments. This highlights the value of exploring complementary design schemes that integrate material and structural considerations to enhance adaptability, ease of construction, and long-term performance under various working conditions.

In response to the challenges, the pre-cast epoxy asphalt cured track (PEACT) has been developed as an innovative solution [8–11]. PEACT combines prefabricated modular blocks made of dry-mixed rubberized epoxy asphalt mixtures (DREAMs) with a concrete base to form a semi-rigid track structure. As shown in Fig. 1(a) and Fig. 1(b), these blocks are cast and cured off-site [9] and then transported to the construction site for rapid installation [12]. This approach offers high structural integrity and stable damping characteristics [13]. Moreover, by adjusting the rubber content in the DREAMs, the dynamic stiffness and damping properties of each block can be flexibly tailored, allowing for a customized vertical stiffness profile along the transition zone [8]. Such

* Corresponding author.
E-mail address: chenguangshi@cqjtu.edu.cn (C. Shi).

https://doi.org/10.1016/j.trgeo.2025.101879
Received 1 September 2025; Received in revised form 15 December 2025; Accepted 25 December 2025
Available online 26 December 2025

modular adaptability makes PEACT particularly suited for mitigating stiffness mismatches under diverse engineering conditions.

PEACT has been extensively evaluated through experimental and numerical studies, consistently demonstrating excellent performance. Shi et al. [9] first proposed PEACT to reduce substructure vibrations in HSR trackbeds while maintaining high performance and adaptability. The basic unit design, dimensions (Fig. 1(a) and Fig. 1(b)), gradation of DREAMs, and methods of incorporating crumb rubber were introduced in their study, with the final design methodology established in Ref. [14] using the volumetric mix-design method (V-S method) [15,16]. Subsequently, DREAMs with four rubber contents (i.e., EA-6 CR, EA-4 CR, EA-2 CR, and EA-0 CR, corresponding to rubber contents of 6 %, 4 %, 2 %, and 0 %, respectively) were developed and tested. Laboratory tests under repeated train loads showed cumulative deformation below 1.5 mm, confirming their long-term durability [9]. Additional evaluations characterized DREAMs as highly resilient materials with excellent cracking resistance, as well as outstanding high- and low-temperature performance [9,11]. To meet on-site construction requirements (e.g., the lifting process in Fig. 1(a)), special asphalt mortars were developed [12,17], and the mechanical behavior during installation was assessed through numerical simulations [12], confirming structural integrity during handling and long-term service. The dynamic behaviors [8–10] and vibration attenuation ability [14] of DREAMs were further investigated using 3D finite element (FE) simulations. Results showed that the inclusion of crumb rubber reduced train-induced stress, strain, and vibration, thereby protecting the substructure while preserving material performance. Specifically, 3D FE simulations in Ref. [8] demonstrated that adjusting the type, number, and arrangement of blocks significantly improves longitudinal stiffness distribution and smooths dynamic responses across the transition zone compared to polyurethane-based transitions, which have been used in practice [18–22]. In addition, compared to traditional slab or ballasted transition zones, PEACT offers greater design flexibility, enabling stiffness gradation through fixed, variable, or stepped stiffness block configurations.

Despite these advantages, existing research has primarily focused on material behavior and basic performance validation. A critical gap remains in the systematic optimization of block layouts, particularly in achieving balanced performance across multiple objectives and accounting for dynamic responses in various track components. To fully exploit the potential of PEACT in transition-zone applications, a surrogate-assisted, data-driven optimization framework is needed that can efficiently explore design alternatives within a feasible computational cost.

In recent years, optimization algorithms have gained increasing prominence in engineering design. For example, Emil et al. [6] applied the Non-dominated Sorting Genetic Algorithm II (NSGA-II) to optimize stiffness and sleeper spacing in a ballasted-slab track transition zone, aiming to reduce wheel-rail forces and base pressures. Shen et al. [23,24] developed a digital twin approach for real-time monitoring and adjustment of track stiffness, covering the entire lifecycle from design to maintenance. These studies highlight the potential of combining machine learning with an optimization algorithm for designing transition zones. This potential is particularly relevant for systems like PEACT, whose modular reconfiguration and tunable material properties enable flexible configuration.

Building on this concept, the present study proposes a proof-of-concept surrogate-assisted optimization framework that integrates FE simulations, a neural-network-based surrogate model, and the NSGA-II algorithm to optimize the performance of the PEACT transition zone. The neural network is trained using FE-generated data and then employed as a static surrogate predictor to efficiently evaluate candidate configurations during the optimization process, thus integrating existing numerical and data-driven methods into an application-oriented framework for a newly developed track system, i.e., the PEACT transition zone.

The paper is organized as follows: Section 2 introduces the background and methodology, including the problem definition, FE modeling, and overall optimization framework. Section 3 details the data preparation procedures. Section 4 presents the optimization process using back propagation (BP) neural networks and NSGA-II algorithms. Section 5 discusses potential improvements and possible extensions. Section 6 summarizes the study and highlights its practical implications for designing transition zones.

Methodology

Problem statement

The ultimate objective of this study is to minimize dynamic response variations within the PEACT transition zone. As a case study, we focus on the transition from a general track section to a bridge section, as illustrated in Fig. 1(c). Following the approach in Ref. [8], variations in

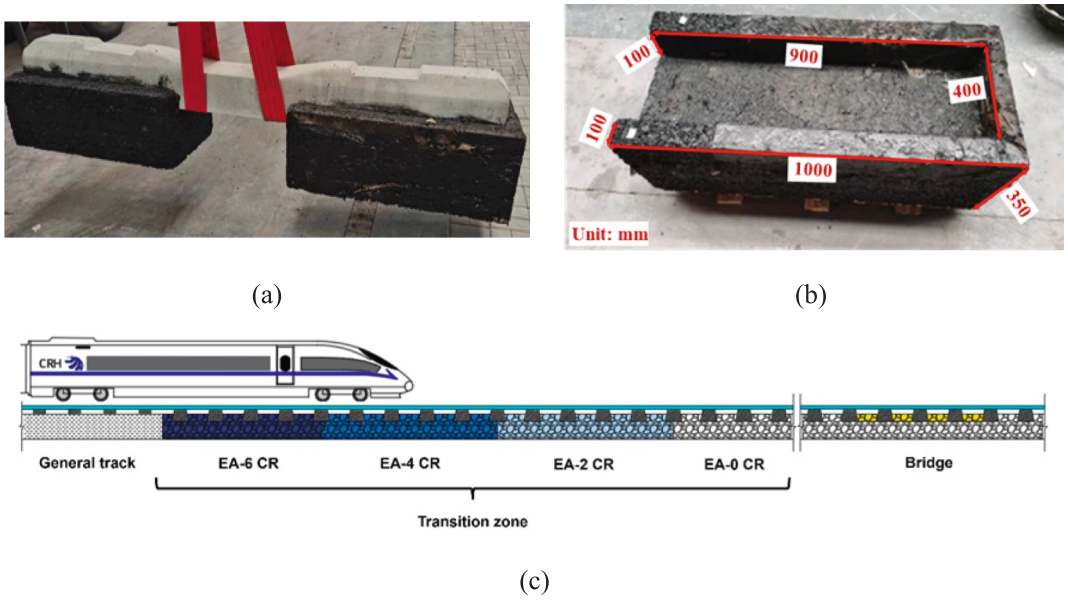

Fig. 1. Schematic of (a) basic unit of PEACT, (b) DREAM blocks, and (c) combination approaches of DREAMs when applied to PEACT transition zone.

dynamic responses along the longitudinal direction of PEACT are characterized using fitting equations. These equations have no direct physical interpretation; instead, they serve solely to quantify the degree of variation. For this reason, linear fitting equations are adopted [25], as their parameters (i.e., slope k and fitting coefficient of determination R^2) provide an intuitive means of assessing smoothness.

Within this framework, the optimization objectives are the slopes k_i and coefficients of determination $R^2{}_i$ for different dynamic responses. The goal is to minimize k_i while maximize $R^2{}_i$, as expressed in Eq. (1) and Eq. (2):

$$min_{x\in D}k_i(x_j), i = 1, 2, \cdots, 13; j = 1, 2, 3, 4\# \tag{1}$$

$$max_{x\in D}R^2{}_i(x_j), i = 1, 2, \cdots, 13; j = 1, 2, 3, 4\# \tag{2}$$

For each k and R^2, their value can be calculated by Eq. (3) ~ Eq. (5):

$$Y_j = F_i(x_1, x_2, x_3, x_4, l_j), j = 1, 2, \cdots, 50\# \tag{3}$$

$$k_i = \frac{\sum_{j=1}^{50} l_j Y_j - n\bar{l_j}\overline{Y_j}}{\sum_{j=1}^{50} l_j^2 - n\bar{l_j}^2}\# \tag{4}$$

$$R_i^2 = \frac{\sum_{j=1}^{50} l_j Y_j - n\sum_{j=1}^{50}\frac{l_j}{n}\sum_{j=1}^{50}\frac{Y_j}{n}}{\sqrt{\left[\sum_{j=1}^{50} l_j^2 - n\left(\sum_{j=1}^{50}\frac{l_j}{n}\right)^2\right]\left[\sum_{j=1}^{50} Y_j^2 - n\left(\sum_{j=1}^{50}\frac{Y_j}{n}\right)^2\right]}}\# \tag{5}$$

Here, Y_j denotes the value of the i-th dynamic response at the j-th cross-section in the PEACT transition zone, and $F_i(\cdot)$ is the mapping from the number and the arrangement of asphalt blocks to the i-th dynamic response, as determined by the numerical model (Section 2.2). The term l_j represents the distance from the j-th cross-section to the general track, and $n = 50$ is the total number of cross sections (see Fig. 2(a)), corresponding to the cross-sections in the numerical model.

The variables x_1, x_2, x_3, x_4 denote the number of DREAM blocks of types EA-6CR, EA-4CR, EA-2CR, and EA-0CR, respectively (following Ref. [8]). From the general track section (softer side) to the bridge section (stiffer side), the baseline arrangement is general section → EA-6CT → EA-4CR → EA-2CR → EA-0CR → bridge section. The exact numbers x_1 x_4 are determined via optimization. For brevity, the general track section is modeled with EA-6CR material.

The notation $x_1 - x_2 - x_3 - x_4$ describes the sequence of DREAM block counts from the softer side to the stiffer side. For example:

- **10–20-10–10:** 10 EA-6CR, 20 EA-4CR, 10 EA-2CR, 10 EA-0CR blocks.
- **5–5–5–5:** 5 of each DREAM type, leaving 30 general track sections before the EA-6CR section.

If the total number of DREAM blocks is less than 50, the remaining x_0 blocks are modeled as general track sections of the softer side, with the following physical constraint:

$$\begin{cases} x_0 + x_1 + x_2 + x_3 + x_4 = n \\ x_1, x_2, x_3, x_4 \in N \end{cases}\# \tag{6}$$

For each configuration $x_1 - x_2 - x_3 - x_4$, the slopes k_i and $R^2{}_i$ are evaluated, forming a typical multi-objective optimization problem. The dataset used for optimization comprises 13 structural dynamic response parameters, computed using the FE model for 341 different cases (see Section 3.2).

FE model of PEACT

Brief introduction of model settings

Fig. 2 illustrates the basic configuration of the proposed numerical model, comprising the dynamic model (Fig. 2(a)), an overview of the model (Fig. 2(b)), and a typical cross-section (Fig. 2(c)). The DREAM blocks are modeled using the generalized Maxwell model [26], implemented in ABAQUS via the Prony series representation [27–29]. In the dynamic models, this layer is equivalent to a series of springs and dampers, as shown in Fig. 2(a). Detailed model settings, such as DREAM gradation, Prony series coefficients, geometric dimensions, and solution parameters, are provided in Ref. [8].

Compared with the model in Ref. [8], several modifications were introduced to improve both accuracy and computational efficiency:

- **Model domain selection.** Previous studies [1,8] showed that train direction has minimal influence on the dynamic response of the PEACT transition zone. Therefore, only the track section labeled "3″ in Fig. 2(b) is used for subsequent analysis.
- **Boundary condition.** Viscous boundaries are applied to the softer side of the model (general track section) to minimize artificial wave reflections from the model boundaries [30].
- **Contact modeling.** A penalty contact formulation is adopted for the interfaces between track components, as described in Ref. [1].
- **Model damping.** The Raleigh damping is used for DREAMs, with coefficients α and β calculated from the damping ratio ζ, which is given in Ref. [31]. Damping of other solid elements is excluded.

Model validation

Since PEACT has not yet been implemented in engineering practice, validation of the numerical model is conducted using field measurement data from pre-cast polyurethane trackbeds. These trackbeds have been successfully applied on the Yinchuan-Xi'an (Yin-Xi) HSR line, which operates at speeds up to 300 km/h, and have demonstrated excellent in-service performance [10]. The only distinction between the pre-cast polyurethane trackbed and PEACT lies in the material properties. According to Chen et al. [32], the mechanical behavior of polyurethane can also be represented by a generalize Maxwell model, making it directly compatible with the modeling framework used for DREAM blocks.

Model validation is performed by comparing the simulated results with field measurements of (i) track stiffness, as shown in Fig. 3(a), and (ii) the peak values of vertical stress at the surface layer, as shown in Fig. 3(b). Track stiffness measurements follow the procedure specified in TB 10082–2017 [33], with further details available in Ref. [8].

The trackbed stiffness measured in the field is approximately 89.90 kN/mm, while the numerical simulation yields 93.75 kN/mm, a difference of less than 5 %. For dynamic response comparison, the simulation is configured to match the actual conditions of the Yin-Xi HSR, with all track blocks modeled as polyurethane (Prony series parameters from Ref. [32]) and a train speed of 300 km/h. The simulated maximum vertical stress at the top of the bottom layer of the pre-cast polyurethane trackbed is 17.8 kPa, differing by only 4.49 % from the measured value of 17.0 kPa. These results confirm that the numerical model is reliable and can be confidently applied to further analyses by replacing polyurethane parameters with those of the four DREAM types.

Optimization process

The overall optimization process is illustrated in Fig. 4. First, the numerical model is employed to generate a dataset covering multiple design cases. For each case, dynamic responses are collected at 50 cross sections in the transition zones. The longitudinal variation of these responses fits with a linear equation, establishing the relationship between the parameter vector $\boldsymbol{x} = (x_1, x_2, x_3, x_4)$ and the corresponding $\boldsymbol{k_i}$, $\boldsymbol{R^2}_i$. In parallel, the same dataset is used to develop a base neural network (denoted as NN-I thereafter) for predicting dynamic response, serving as

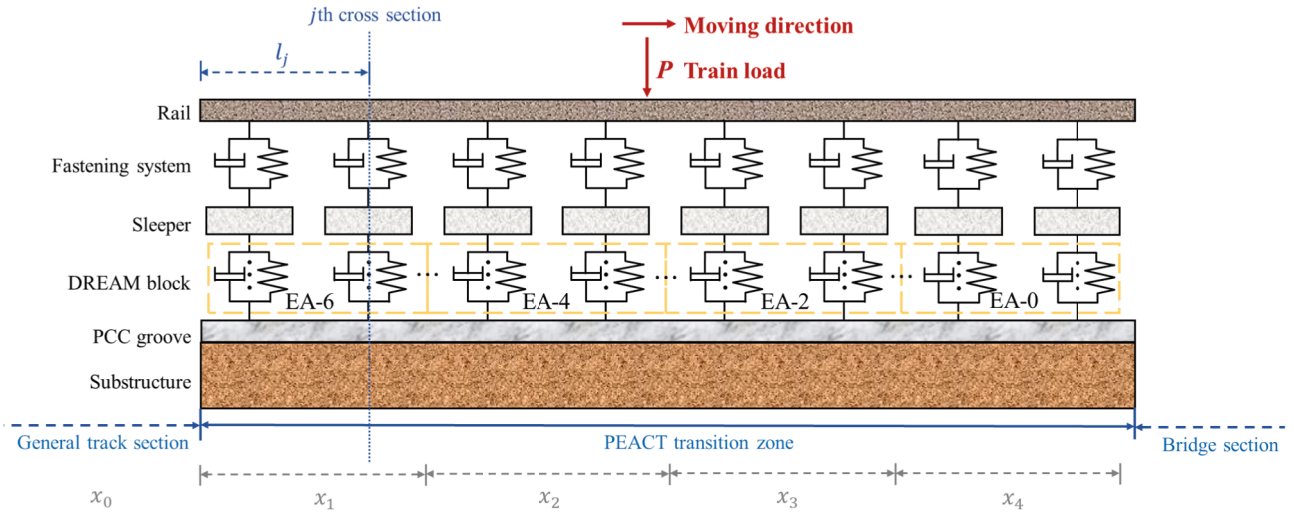

(a)

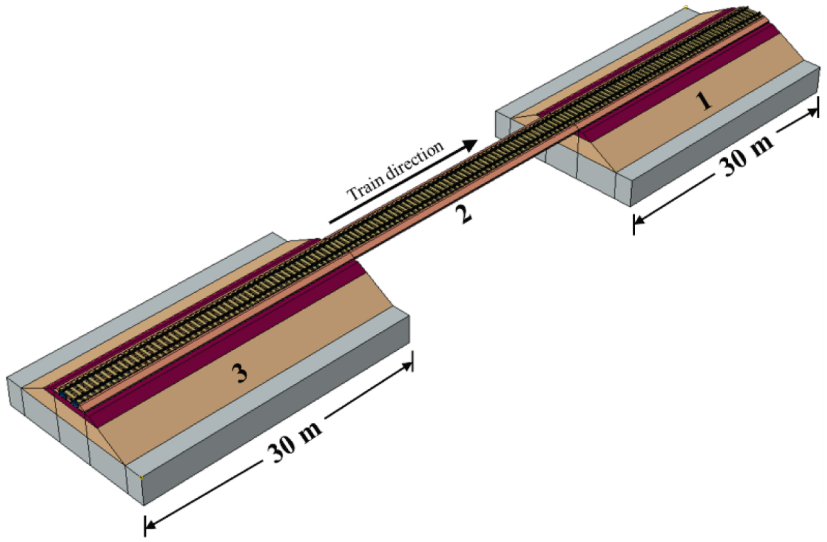

(b)

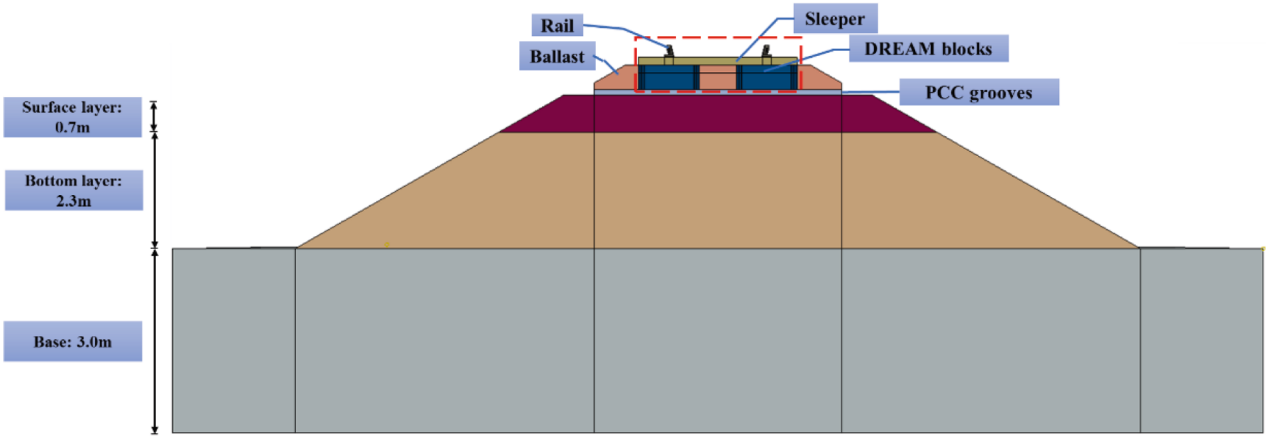

(c)

Fig. 2. Schematic of (a) dynamic model of PEACT transition zone, (b) overview of PEACT transition zone FE model, and (c) typical cross-section of PEACT with DREAM blocks.

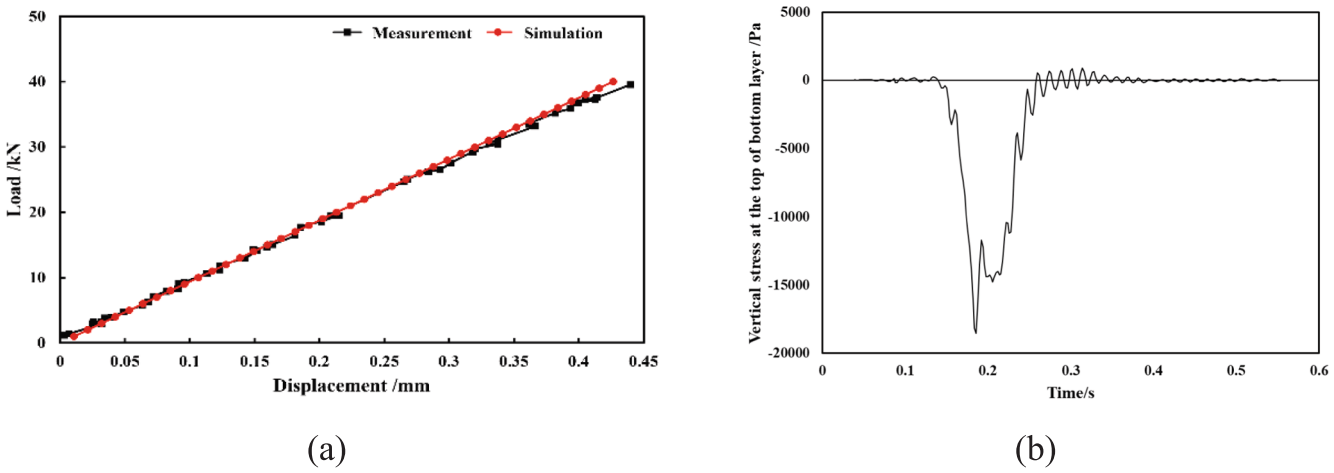

Fig. 3. Schematic of (a) comparison between simulated track stiffness and measured stiffness, and (b) simulated dynamic response (taking vertical stress at the top of the bottom layer as an example).

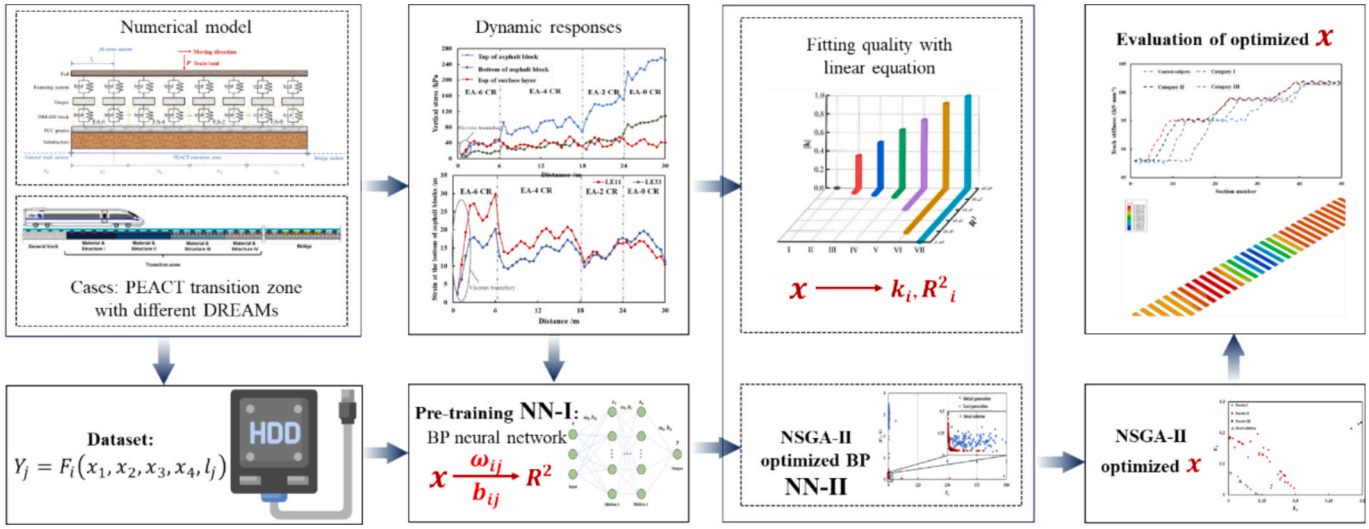

Fig. 4. Workflow of optimization process.

the data source for NSGA-II optimization. A six-layer BP neural network is selected for its proven applicability in engineering problems and its ability to update numerical parameters [34], with detailed settings provided in Section 4.2. However, NN-I's generalization capability is limited because key training parameters, such as the number of neurons per hidden layer, training sample size, and learning rate, are not physically guided. To address this, the NSGA-II algorithm (see Appendix A) is applied to optimize these parameters, producing an NSGA-II-optimized BP neural network (denoted as NN-II thereafter). NN-II is then used as the data source for the final NSGA-II-based optimization of the PEACT transition zone design. Finally, the numerical model compares the dynamic responses of the DREAM block arrangements before and after optimization, evaluating the feasibility and effectiveness of the proposed scheme.

Data preparation

As a novel track structure, PEACT transition zones currently lack standardized regulations for characterizing their dynamic behavior. To address this, and considering structural behavior and material performance, the relevant Chinese regulations [33], and key parameters from pavement engineering [35], this study selects 13 dynamic response parameters to provide the most comprehensive possible description of PEACT behavior under train loading. These parameters and their abbreviations are listed in Table 1. Accordingly, the slope vector is expressed as $\boldsymbol{k} = (k_m)$ and the coefficient-of-determination vector as $\boldsymbol{R}^2 = (R^2{}_m)$, where m corresponds to the parameters in Table 1. The selected parameters reflect four complementary aspects of the PEACT

Table 1
Selected parameters for describing the dynamic characteristics of PEACT.

Structural layer	Response location	Response	Abbreviation
Rail	Top	Vertical acceleration	R_A2
		Vertical displacement	R_U2
Sleeper	Top	Vertical acceleration	S_A2
Surface layer	Top	Vertical acceleration	SL_A2
		Vertical stress	SL_S22
		Vertical displacement	SL_U2
DREAM blocks	Top	Vertical acceleration	AB_T_A2
		Vertical stress	AB_T_S22
		Vertical displacement	AB_T_U2
	Bottom	Vertical stress	AB_D_S22
		Vertical acceleration	AB_D_A2
		Lateral strain	AB_D_LE11
		Longitudinal strain	AB_D_LE33

transition zone:

- **Dynamic performance**. Vertical acceleration and displacement at the rail top are included, as they represent the vibration transmitted from the vehicle to the track.
- **Vibration attenuation capability**. Accelerations at five key layers (rail, sleeper, top and bottom of asphalt blocks, and top of the surface layer) are considered to evaluate the energy dissipation and damping performance of DREAMs.
- **Structural safety of DREAM blocks.** Longitudinal and lateral strains at the bottom of asphalt blocks are used to assess the potential for cracking or fatigue, in accordance with pavement engineering practice [35].
- **Serviceability and deformation control**. Displacements at the top of the rail, asphalt block, and surface layer are analysed to verify compliance with allowable limits in Chinese railway standards [33].

Influence of design schemes on the transition zone

Longitudinal distribution characteristics of track parameters

As a preliminary study, Ref. [8] systematically examined the longitudinal variation of dynamic responses in the PEACT transition zone using quadratic curves. However, these quadratic equations lack physical interpretation, and the study only considered a single block arrangement, namely 10–20-10–10. In this section, the same arrangement (10–20-10–10) is used to illustrate the feasibility of applying linear fitting equations to the PEACT transition zone. As shown in Fig. 5 and Table 2, vertical stresses at different layers and strains at the bottom of asphalt blocks as examples to demonstrate how linear fitting can effectively capture the variation trends.

Fig. 5(a) shows the longitudinal variation of vertical stresses at three locations: the top of the asphalt block, the bottom of the asphalt block, and the top of the surface layer. All three exhibit a gradual increase along the longitudinal direction, with the steepest rise occurring at the top of the asphalt blocks. This suggests that uneven stress distribution in the PEACT transition zone is concentrated within the asphalt blocks themselves, rather than in the surface layer of the embankment, as is typical for conventional ballast or ballastless trackbeds. As shown in Fig. 5(b), the strain at the bottom of the asphalt blocks increases with higher rubber content, further emphasizing the importance of considering the mechanical behavior of asphalt blocks when optimizing the smoothness of the PEACT transition zone.

It should be noted that the viscous boundary condition assumes zero dynamic response at the boundary elements. As a result, computed values near this boundary may be inaccurate. To avoid such errors, the results from the three cross-sections closest to the boundary were excluded from subsequent analyses.

Table 2
Summary of fitting lines of track parameters.

Parameter	Location	Fitting equation	R^2	WSI
Maximum vertical stress	Top of the asphalt block	$y = 7611x - 2715$	0.8793	0.9196
	Bottom of the asphalt block	$y = 2871x - 167.5$	0.8193	0.9941
	Top of the surface layer	$y = 302x - 33346$	0.0856	0.9833
Maximum lateral strain (LE11)	Bottom of the asphalt block	$y = -0.224x + 20.3$	0.1572	0.8473
Maximum longitudinal strain (LE33)	Bottom of the asphalt block	$y = -0.174x + 12.1$	0.1217	0.9388

Table 2 summarizes the fitting results for the five dynamic responses. For vertical stresses, the R^2 values decrease with the measurement depth in the track structure. However, this does not invalidate the use of linear fitting in this study. The numerical model is subjected to high-speed train loads containing multiple frequency components [8,36,37], causing substantial variation in the loads experienced by different cross-sections as the train passes. The vibration attenuation of the asphalt blocks amplifies these relative variations, making deeper measurement points more sensitive to uneven distribution. Nevertheless, the slope of the fitted line still reflects the overall trend. Moreover, due to the attenuation effect, stresses in the surface layer are more evenly distributed on both sides of the fitted line. This is quantitatively supported by the high Weighted Symmetry Index (WSI) values in Table 2, calculated using Eqs. (7)~(9):

$$WSI = 1 - \frac{|S_+ - S_-|}{|S_+ + S_-|}\# \tag{7}$$

$$S_+ = \sum_{r_i>0} r_i^2, S_+ = \sum_{r_i<0} r_i^2\# \tag{8}$$

$$r_i = y_i - \hat{y}_i\# \tag{9}$$

where y_i is the simulated value from the numerical model. $\hat{y}_i$ is the fitted value. r_i is the residual. S_+ and S_- are the sums of squared residuals in the positive and negative sides of the fitted line, respectively. WSI values range from 0 to 1, with values close to 1 indicating a balanced distribution of residuals, and values close to 0 indicating a strong bias.

For the strains (LE11 and LE33), the behavior is different. As shown in Fig. 5(b), two junctions appear (at EA-6CR to EA-4CR and EA-4CR to EA-2CR) due to notable stiffness differences between these materials. No clear junction is observed from EA-2CR to EA-0CR because of their similar mechanical properties [8,31]. Consequently, the R^2 and WSI values for these two parameters are lower than those for vertical

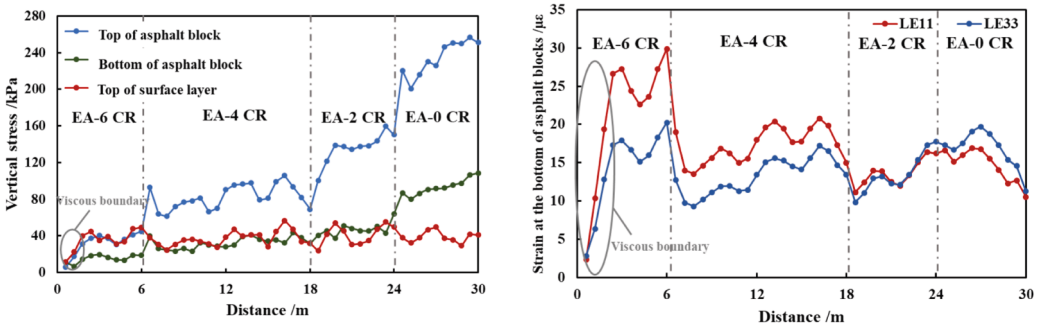

(a) (b)

Fig. 5. Longitudinal distribution characteristics of (a) maximum vertical stress, (b) lateral and longitudinal strain at the bottom of the asphalt block (taking 10–20-10–10 as an example).

stresses. Nonetheless, the linear fitting still captures the overall variation trend and provides a useful reference for defining "smooth change".

Influence of the number of asphalt blocks

This section exams how the number of asphalt blocks (corresponding to the length of the transition zone) affects the dynamic responses. Seven working conditions are evaluated, as listed in Table 3, where the general track section is denoted as EA-6 CR'.

The maximum values of each dynamic response for the considered cases are listed in Table 4, with units of m/s^2 for acceleration, Pa for stress, με for strain, and mm for displacement. Results show that varying the number of asphalt blocks has a negligible influence on these maximum values, suggesting that each type of DREAM performs independently in the transition zone, largely unaffected by its position within the structure. When dynamic response values in the transition zone are relatively high, some variation is observed in the maximum vertical stress. Specifically, as the total number of asphalt blocks in the last four sections decreases, the maximum vertical stress also tends to decrease. This indicates that, from a stress-reduction perspective, shorter transition zones are preferable. However, a reduction in the number of blocks also leads to an increase in maximum strain at the top of the asphalt blocks, implying that shorter transition zones subject the blocks to greater deformation loads. Overall, both longer and shorter transition zones yield dynamic response levels within acceptable limits. Therefore, optimizing transition zone design solely to minimize these response levels offers limited benefits, and alternative design strategies should be explored.

For assessing the overall longitudinal variation trend, k and R^2 are used to evaluate each design scheme. To eliminate the influence of absolute values, normalization is first applied to each case for better comparison, as shown in Eq. (10):

$$x' = \frac{x - \min(x)}{\max(x) - \min(x)}\# \tag{10}$$

where x' is the normalized k or R^2. x, $\min(x)$, and $\max(x)$ are original, minimum, and maximum values, respectively.

Taking the accelerations at five locations as an example, Fig. 6 illustrates the influence of the number of asphalt blocks. Only the k and R^2 values of vertical acceleration at the top of the rail increase consistently as the transition zone length decreases, indicating a stronger linear trend but with a steeper slope. In contrast, k and R^2 for other locations show no clear relationship with the transition zone length. To achieve smooth dynamic response changes, the slope k of the fitted line should be as small as possible, ensuring both smooth train passage and effective protection of the trackbed. However, the results show that for the seven tested configurations, maximizing R^2 often coincides with an increase in k. This trade-off makes it challenging to determine an optimal transition zone length based on the current results. Therefore, a comprehensive comparison is required to select a design that minimizes the k while maximizing R^2.

Table 3
Working conditions affected by the number of asphalt blocks.

Type of asphalt block	EA-6 CR' (x_0)	EA-6 CR (x_1)	EA-4 CR (x_2)	EA-2 CR (x_3)	EA-0 CR (x_4)
I	2	12	12	12	12
II	6	11	11	11	11
III	10	10	10	10	10
IV	14	9	9	9	9
V	18	8	8	8	8
VI	22	7	7	7	7
VII	26	6	6	6	6

Influence of the arrangement method of asphalt blocks

In addition to the transition zone length, the arrangement method is another key factor in the optimization process. This section examines four working conditions with different arrangement configurations, as summarized in Table 5.

Similar to the discussion on the influence of transition zone length, this section first examines the effect of arrangement patterns on the maximum dynamic response values, as summarized in Table 6. The results indicate that, like the effect of the number of asphalt blocks, the arrangement pattern does not significantly influence the maximum dynamic response. However, unlike the variation observed with different transition zone lengths, the differences between arrangement patterns are almost negligible. This can be explained by the load transfer mechanism in the track structure: train loads are primarily distribution over approximately five adjacent sleepers and then transmitted to the lower layers [38]. In all four arrangement patterns considered, each type of DREAM is laid over at least 10 consecutive sections. As a result, every section contains multiple segments that accurately reflect the mechanical properties of its corresponding DREAM type, resulting in similar maximum dynamic response values across the different arrangement patterns.

Furthermore, the normalized k and R^2 values for the five acceleration measurement locations are presented in Fig. 7. Similar to findings for maximum dynamic responses, neither k and R^2 shows a clear correlation with the arrangement pattern. Nonetheless, arrangement I, i.e., 20–10–10–10, yields the highest k and R^2 values at most positions, suggesting that the longitudinal variation of dynamic responses is relatively smooth under this configuration. An exception is observed at the top of the asphalt block, where arrangement I produces the lowest k and R^2 values. This indicates that, while Arrangement I performs well overall, it does not provide uniformly ideal results across all measurement points. Therefore, to achieve balanced performance for all five acceleration parameters, a tailored arrangement strategy for the four DREAM types is necessary, even when the total number of asphalt blocks is fixed.

Step 0: Data set

Integrating the analysis in Section 3.1, it is evident that neither the total number of asphalt blocks nor their arrangement pattern shows a significant correlation with the trends in variation of dynamic responses. Moreover, the preceding sections considered only five acceleration parameters out of the 13 dynamic response parameters. When all 13 parameters are included, identifying a design scheme that achieves uniformly smooth transitions across all responses becomes more challenging. This complexity suggests that, for design purposes, the variation patterns of these 13 parameters should be treated as a "black box", with optimization carried out based on sufficiently large and representative datasets.

To this end, 341 randomly generated working conditions satisfying Eq. (6) were simulated using the numerical model. Each condition yields 13 dynamic response parameters, producing 26 output values (k and R^2 for each parameter). By contrast, the model's input space consists of only four variables representing the number of each type of asphalt block. This imbalance between a small set of input variables and a large set of output targets poses two challenges: (1) fitting a neural network would require a substantial dataset to achieve adequate accuracy, and (2) directly using all outputs as objectives in NSGA-II optimization would increase computational complexity and reduce optimization efficiency [39].

To address this, the dataset was first grouped according to the characteristics of the 13 dynamic response parameters, as summarized in Table 7. For each group, a separated neural network was trained for each parameter. To maintain generalization capability, the 341 cases were randomly split into training and validation sets with a 7:3 ratio in each training session.

Table 4
Effect of the number of asphalt blocks on the maximum value of the track parameters in the transition zone.

	SL_A2	SL_U2	SL_S22	AB_T_A2	AB_T_S22	AB_T_U2	AB_D_A2	AB_D_S22	AB_D_LE11	AB_D_LE33
I	17.40	0.48	52861.50	22.79	192678.75	0.52	17.84	53310.93	27.00	25.04
II	17.40	0.48	53321.55	22.79	185316.00	0.52	17.84	53314.06	27.00	25.07
III	17.55	0.48	53318.70	22.79	172650.75	0.52	17.84	53323.46	27.00	25.05
IV	17.55	0.48	53319.00	22.82	172649.25	0.52	17.85	53335.44	27.00	25.07
V	17.55	0.48	53296.20	22.90	172649.25	0.52	17.97	53317.83	27.00	25.04
VI	17.55	0.48	53936.70	22.90	172643.25	0.52	17.97	53313.14	27.45	25.04
VII	17.55	0.48	53937.23	22.90	169181.25	0.52	17.97	53282.69	27.45	40.93

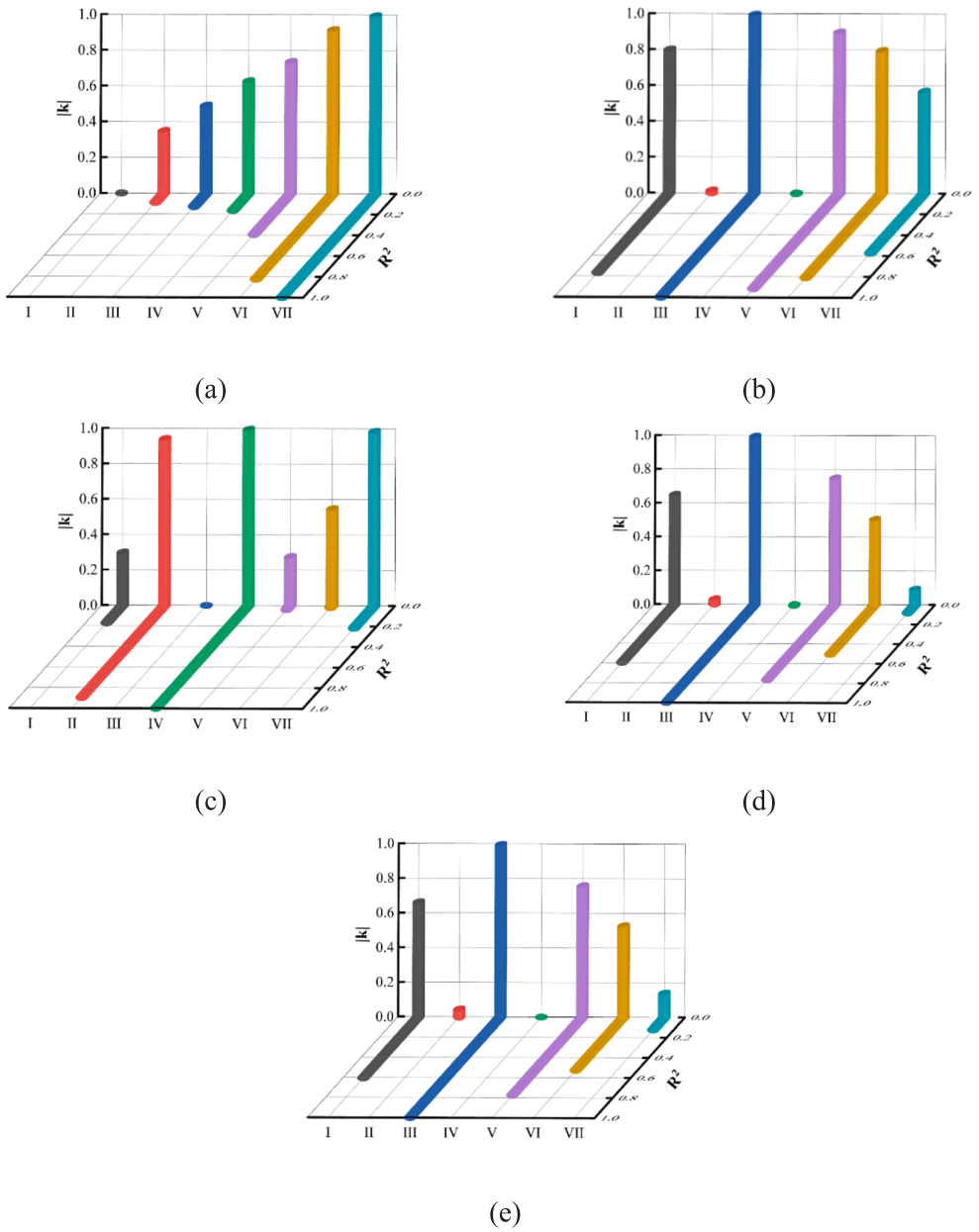

Fig. 6. Slope and R^2 of longitudinal change in acceleration after normalization the influence of the number of asphalt blocks (a) at the top of rail (R_A2), (b) at the top of sleeper (S_A2), (c) at the top of asphalt blocks (AB_T_A2), (d) at the bottom of asphalt blocks (AB_D_A2), and (e) at the top of surface layer (SL_A2).

Optimization process

Step 1: Pre-training for predicting dynamic responses in the transition zone (NN-I)

The core of NN-I is a six-layer BP neural network, with an input layer of four neurons (x_1 x_4) and an output layer of two neurons (k and R^2). The four hidden layers contain 32, 64, 128, and 32 neurons, respectively. A hyperbolic tangent (tanh) function is used as the activation function for all layers, and the learning rate is set to 0.01. The training process terminates when either the loss function falls below 0.001 or the number of training iterations exceeds 2000. Taking four dynamic re-

Table 5
Working conditions affected by the arrangement method of asphalt blocks.

Number of asphalt blocks	10 (x_0)	10 (x_1)	10 (x_2)	10 (x_3)	10 (x_4)
I	EA-6 CR	EA-6 CR	EA-4 CR	EA-2 CR	EA-0 CR
II	EA-6 CR	EA-4 CR	EA-4 CR	EA-2 CR	EA-0 CR
III	EA-6 CR	EA-4 CR	EA-2 CR	EA-2 CR	EA-0 CR
IV	EA-6 CR	EA-4 CR	EA-2 CR	EA-0 CR	EA-0 CR

sponses as examples, the corresponding loss curves are shown in Fig. 8.

The loss curves of all individual dynamic response prediction networks converge to relatively small values (approximately 0.01) after a limited number of iterations, but fail to meet the preset target of 0.001. This necessitates further verification of their predictive accuracy. Fig. 9 compares the predicted and actual values of NN-I on the validation set. While some responses, such as AB_D_A2 and AB_T_U2, show good agreement with the fitted R^2 values of 0.88 and 0.91, others, such as R_A2 and SL_S22, perform poorly, with R^2 values of only 0.47 and 0.44, respectively. The fitted R^2 values for all remaining networks are listed in Table 8.

The results indicate that using fixed, pre-set training parameters cannot achieve consistently high accuracy across all dynamic response predictions. Similar to FE model calibration, manually tuning neural network parameters for each case would require substantial computational effort and still might not yield optimal settings. Therefore, the enhance NN-I before applying it to the PEACT transition zone optimization, this study employs NSGA-II to automatically optimize the key training parameters, as detailed in Section 4.2.

Step 2: Establish the NSGA-II-BP network (NN-II)

To mitigate the risk of overfitting given the moderate dataset size (341 FE samples), the 13 response parameters were not modeled using a single high-dimensional network. Instead, they were divided into three independent groups (as detailed in Table 7) and learned using three NN-II surrogates. This strategy significantly reduces the output dimensionality per model and limits the total number of trainable parameters, improving training stability and generalization.

When optimizing NN-I with NSGA-II, the goal is to tune six training parameters (i.e., the number of neurons in each of the four hidden layers, the sample size for each training session, and the learning rate, denoted as x_1 x_6, respectively). The optimization aims to simultaneously minimize the training time to reach the target loss value of 0.001 (F_1) and maximize the prediction accuracy in terms of R^2 (F_2), as formulated in Eqs. (11) ~ (12):

$$min_{x\in D}F_1(x_i), i = 1, 2, \cdots, 6\# \tag{11}$$

$$max_{x\in D}F_2(x_i), i = 1, 2, \cdots, 6\# \tag{12}$$

Here D represents the feasible domain of the training parameters:

- For x_1 x_4 (neurons in hidden layers), $x_i \in [4, 16]$ and $x_i \in N$.
- For x_5 (sample size per training), $x_5 \in [8, 64]$ and $x_5 \in N$.
- For x_6 (learning rate), $x_6 \in [0.001, 0.01]$.

Since NSGA-II minimizes objective functions, Eq. (12) is reformulated as:

$$min_{x\in D}|F_2(x_i) - 1\,|, i = 1, 2, 3, 4\# \tag{13}$$

In the NSGA-II framework, each individual encodes a complete set of training parameters for NN-I and represents a fully trained neural network. In this study, each generation contains 200 individuals, evolving over 50 generations, resulting in a total of $200 \times 50 = 10000$ network trainings. The number of neurons in each hidden layer is treated as a tunable parameter within the range of 4–16. Under these settings, each NN-II contains on the order of 10^3 trainable parameters, which is modest relative to the available training data volume and consistent with common practice in surrogate-assisted engineering optimization [6]. To further control model complexity and avoid overfitting, the dataset is divided into training and validation subsets with a proportion of 7:3. The loss curves in Fig. 8 indicate that NN-I converges to a stable value within 500 iterations. Therefore, for efficiency, each NN-I in the optimization process is trained for 500 iterations rather than until the full convergence threshold of 0.001 is met. Under these settings, NSGA-II was applied to optimize the neural networks predicting changes in four representative parameters, i.e., R_A2, AB_D_A2, AB_T_U2, and SL_S22. The results are presented in Fig. 10.

As shown in Fig. 10, the Pareto fronts progressively converge toward the origin over generations, indicating stable convergence of the NSGA-II optimization under the adopted parameter settings. In addition, several independent runs with different random seeds were performed, and similar Pareto fronts and optimal solutions were consistently obtained, indicating that the optimization results are not sensitive to stochastic initialization.

After applying NSGA-II to optimize NN-I, the Pareto front of the population gradually converges toward the origin of the coordinate system, indicating the existence of parameter sets that simultaneously minimize NN-I training time and maximize prediction accuracy. In principle, any individual near this origin in the final generation can serve as an optimal solution, and its parameters can be adopted to establish NN-II. Four representative examples of such ideal solutions are shown in Fig. 10. It should be emphasized that, in multi-objective optimization, every point on the Pareto front is theoretically optimal. However, in this study, the primary objective is to enhance NN-I's predictive accuracy for dynamic responses, even if this requires sacrificing some training time. Accordingly, individuals with higher fitting accuracy, as illustrated in Fig. 10(d), are prioritized.

Following this approach, NSGA-II is applied to each NN-I, and the most suitable individual from the final generation is selected as the basis for NN-II. The corresponding optimized training parameters are then used to retrain the networks. Comparable training and validation errors were observed for all NN-II models, indicating satisfactory generalization capability, as detailed in Table 9, in which R_1^2 and R_2^2 are training errors and validation errors, respectively. It should be emphasized that NN-II is employed to capture relative trends and ranking among different design schemes under consistent modeling assumptions, rather than to provide exact absolute predictions of physical quantities. The final optimal configurations identified through surrogate-assisted optimization are subsequently verified using direct FE simulations, as detailed in Section 4.4, thus ensuring the reliability of the design

Table 6
Effect of the arrangement method of asphalt blocks on the maximum value of the track parameters in the transition zone.

	SL_A2	SL_U2	SL_S22	AB_T_A2	AB_T_S22	AB_T_U2	AB_D_A2	AB_D_S22	AB_D_LE11	AB_D_LE33
I	1488.48	1.87	34.43	17.84	0.48	53318.70	22.79	172650.75	0.52	17.55
II	1488.43	1.87	34.44	17.84	0.48	53318.55	22.79	172650.00	0.52	17.40
III	1488.80	1.87	34.44	17.72	0.48	52868.85	22.70	172650.00	0.52	17.40
IV	1488.80	1.87	34.44	17.72	0.48	52868.85	22.70	172695.25	0.52	17.40

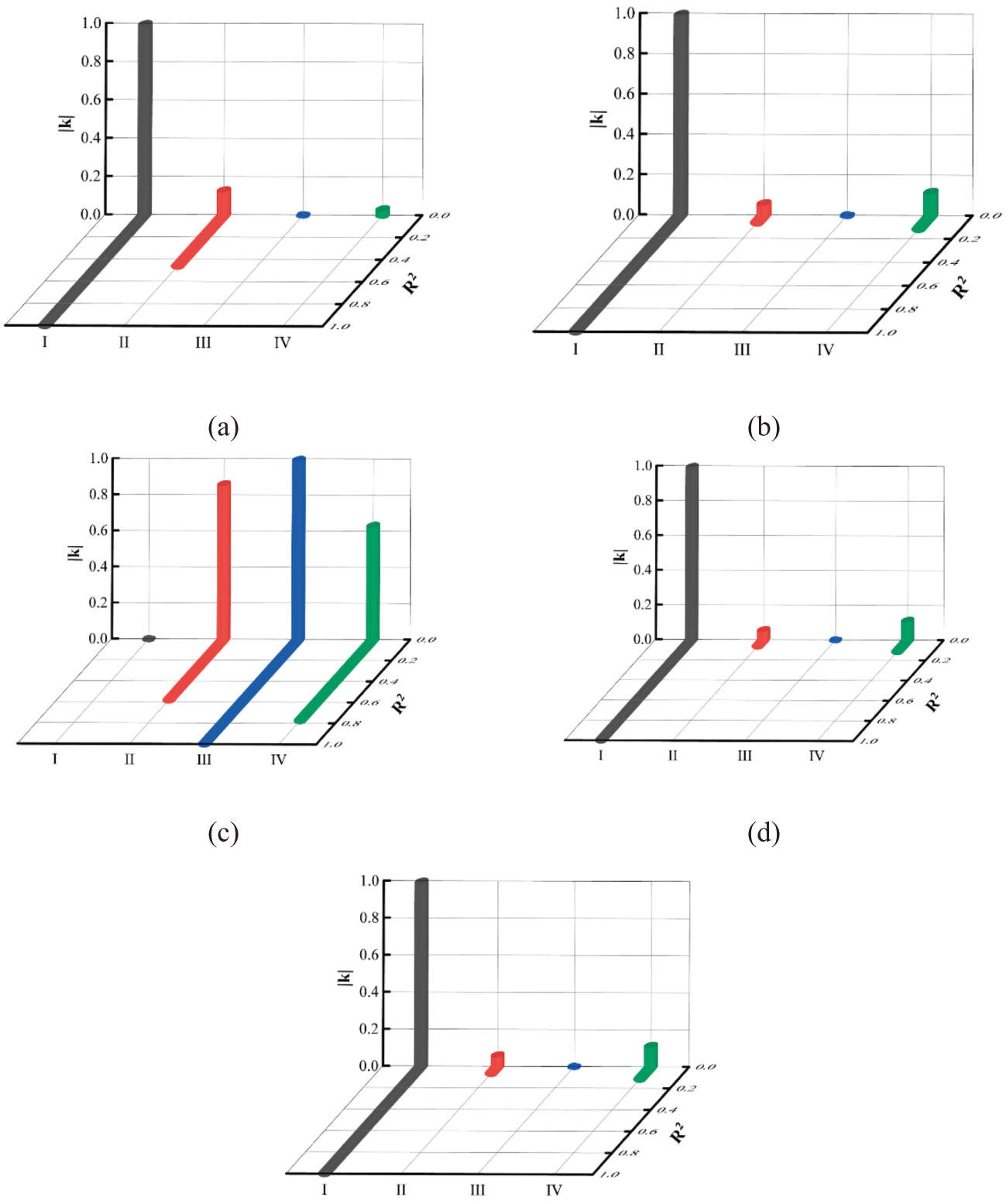

Fig. 7. Slope and R^2 of longitudinal change in acceleration after normalization under the influence of arrangement method of asphalt blocks (a) at the top of rail (R_A2), (b) at the top of sleeper (S_A2), (c) at the top of asphalt blocks (AB_T_A2), (d) at the bottom of asphalt blocks (AB_D_T2), and (e) at the top of surface layer (SL_A2).

Table 7
Categories of track parameters.

Category number	Track parameters	Basis of classification
I	AB_D_LE11, AB_T_S22, AB_T_U2, SL_S22, SL_U2	Structure condition
II	AB_D_LE11, AB_D_LE33, AB_D_S22, AB_T_S22, AB_T_U2	Asphalt block condition
III	AB_D_A2, AB_T_A2, R_A2, S_A2, SL_A2	Track vibration

decisions.

Step 3: Optimize the design scheme of the transition zone

Once the NN-IIs are established, they can efficiently predict longitudinal variations in the dynamic response of PEACT transition zones for various asphalt block arrangements. This capability allows NSGA-II to generate individuals directly from NN-II predictions, thereby avoiding the need for repeated FE simulations.

The optimization problem for the arrangement method was introduced in Section 2.1. Since NSGA-II seeks to minimize objective functions, Eq. (2) is reformulated as:

$$max_{x\in D}\left|R^2{}_i(x_j)-1\right|, i=1,2,\cdots,13; j=1,2,3,4\# \tag{14}$$

For each dataset, the NSGA-II is run with a population size of 50 for 10,000 generations. The optimization objectives comprise ten targets: $k_i(i=1,2,3,4,5)$ and $R^2{}_i(i=1,2,3,4,5)$, denoted as F_1 F_5 and f_1 f_5, respectively, in accordance with Table 7.

Fig. 11 shows the final-generation population distributions for three datasets, using F_1 vs. F_3, and F_3 vs. F_5 as examples, with their Pareto fronts and optimal points marked. After evolution, individuals cluster into three distinct regions, revealing three Pareto fronts that reflect trade-offs among objectives. As discussed in Section 3.1, smaller objective values indicate smoother dynamic response transitions, making the first Pareto front the optimal solution set. To avoid solutions at the extreme edge of the set, which may be sensitive to small perturbations, this study selects individuals near the center of the first Pareto front, and their corresponding asphalt block arrangements are adopted as the final design scheme.

The Pareto fronts in Fig. 11(c1) and Fig. 11(c2) are less distinct than in the previous four cases, indicating that optimizing the five dynamic response parameters in Category III using NSGA-II is more challenging. Moreover, the Pareto fronts shown in Fig. 11 are not strictly single-level fronts, but rather collections of multi-level Pareto fronts with slight differences. Given that each category has ten optimization objectives, non-dominated sorting occurs in a ten-dimensional space, which not only increases computational load but also complicates visualization.

When projecting the population onto the two-dimensional planes in Fig. 11, an individual may appear on the Pareto front in one plane but fall to a lower-level front in another. This phenomenon is evident when comparing Figs. 11(a), 11(b), and 11(c). Therefore, in screening for optimal solutions, an individual doesn't need to lie on the Pareto front in every two-dimensional projection, meaning that being on the Pareto front in most projections is sufficient. Following this principle, the asphalt block arrangements selected for each of the three categories are summarized in Table 10. These arrangements correspond to design priorities focusing on structural working conditions, asphalt block working conditions, and vibration-damping performance, respectively.

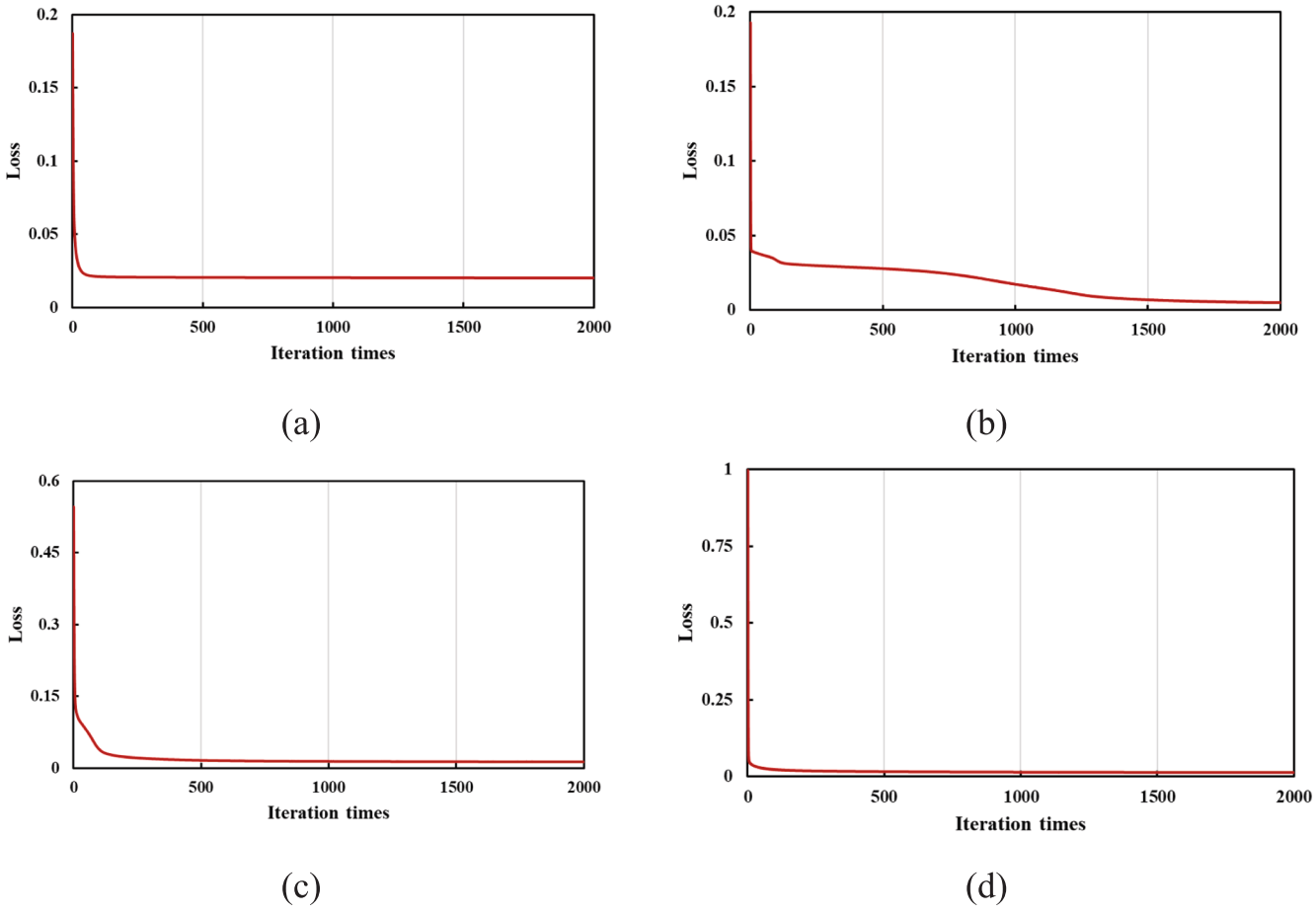

Fig. 8. Loss curves of a typical track parameter, taking (a) R_A2, (b) AB_D_A2, (c) AB_T_U2, and (d) SL_S22 as examples.

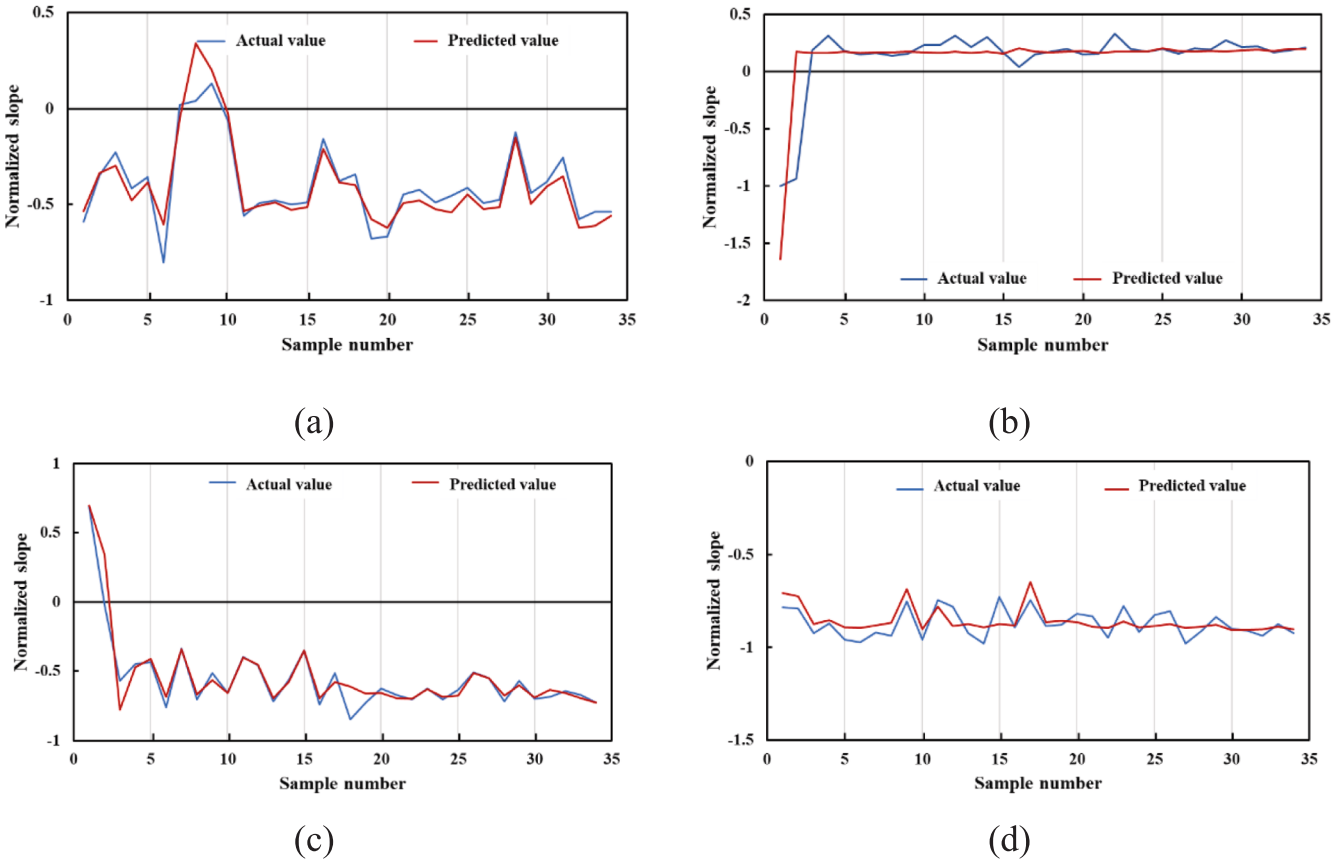

Fig. 9. Accuracy of a typical neural network without optimization, taking the normalized slope of (a) R_A2, (b) AB_D_A2, (c) AB_T_U2, and (d) SL_S22 as examples.

Table 8
Summary of the accuracy of each network before optimization.

	AB_D_A2	AB_D_LE11	AB_D_LE33	AB_D_S22	AB_T_A2	AB_T_S22	AB_T_U2	R_A2	R_U2	SL_A2	SL_S22	SL_U2	S_A2
R^2	0.88	0.73	0.43	0.81	0.72	0.65	0.91	0.47	0.23	0.29	0.44	0.51	0.39

The performance of these three design schemes is evaluated in the following section.

Step 4: Evaluate the optimization results

It should be noted that all optimized design schemes discussed in this section are evaluated using direct FE simulations, ensuring that the reported improvements are independent of surrogate-model approximation errors. To evaluate the three optimized design schemes, the arrangement method from Ref. [8] (10–20-10–10) is adopted as the control case. Corresponding FE models are established for each scheme, and their performance is assessed according to the three design priorities defined in Table 7: structural working conditions (Category I), asphalt block working conditions (Category II), and vibration control (Category III).

The stiffness distributions before and after optimization are shown in Fig. 12. In all cases, the track stiffness increases gradually along the longitudinal direction. Due to material differences, the stiffness values for EA-0CR, EA-2CR, EA-4CR, and EA-6CR cross-sections are approximately 87.76, 95.01, 98.89, and 101.21 kN/mm, respectively. The stiffness within each section fluctuates around these values, producing "plateaus" in the overall trend, while the interfaces between materials exhibit 5 ~ 6 sections of transition.

If plateaus and rising segments alternate frequently, the stiffness change becomes less smooth, potentially impairing train ride quality. Ideally, the distance between two plateaus should be maximized, or the stiffness should rise continuously with minimal plateau areas. As shown in Fig. 12, Category I achieves smoother stiffness transitions by maximizing the spacing between plateaus. At the same time, Category III shortens plateau lengths to complete stiffness changes over the smallest possible distance. Category II shows no clear advantage in stiffness alone. However, stiffness improvement is not the sole design goal: each category must also be evaluated according to its specific optimization priority, which will be discussed in the following subsections.

Fig. 13 illustrates the effects of the three optimized schemes using AB_T_U2, AB_D_S22, and S_A2 as representative examples. For clarity, the dynamic response distributions are shown at specific time points: 0.045 s for Categories I and II (train load above the 9-th cross-section) and 0.139 s for Category III (train load above the central cross-section).

Category I targets the working condition of the entire structure. In the control case, when the train load exceeds the 9th section, the displacement at the top of the asphalt blocks spreads unevenly from the 4th to the 11th block, with irregular peaks between the 10th and 11th blocks. This dispersed pattern indicates uneven load transfer and prolonged structural loading, which may accelerate damage accumulation. In contrast, Category I concentrates the response within blocks 7 ~ 10, showing a smooth rise and fall pattern. This reflects a more uniform load distribution and a reduction in localized unevenness, thereby improving the overall working condition of the structure.

Category II focuses on the working conditions of the asphalt blocks

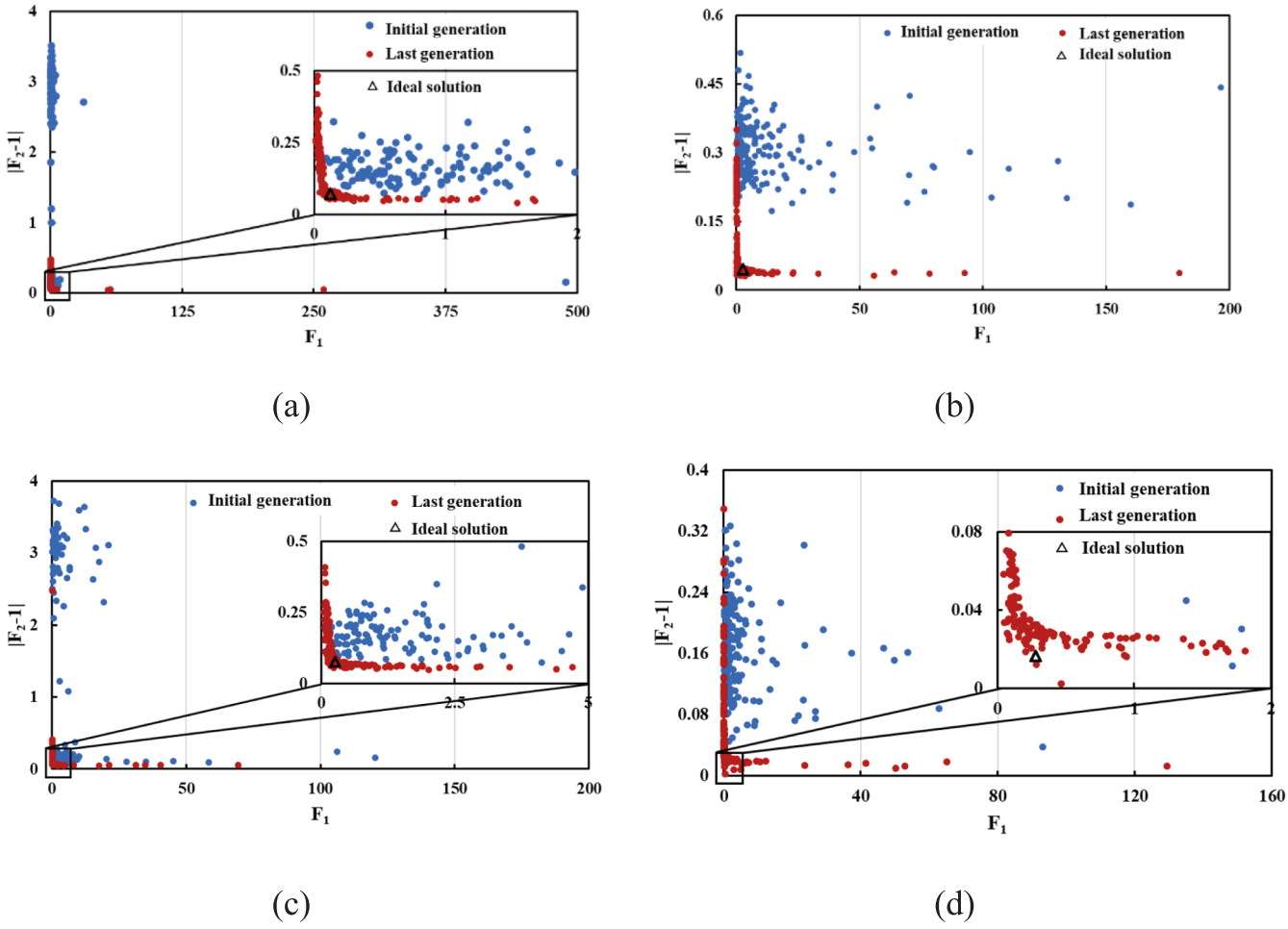

Fig. 10. Establishment of NSGA-II-BP network, taking (a) R_A2, (b) AB_D_A2, (c) AB_T_U2, and (d) SL_S22 as examples.

Table 9
Summary of the accuracy of each network after optimization.

	AB_D_A2	AB_D_LE11	AB_D_LE33	AB_D_S22	AB_T_A2	AB_T_S22	AB_T_U2	R_A2	R_U2	SL_A2	SL_S22	SL_U2	S_A2
R_1^2	0.98	0.93	0.94	0.91	0.95	0.94	0.93	0.93	0.93	0.92	0.94	0.95	0.92
R_2^2	0.96	0.92	0.94	0.91	0.92	0.93	0.93	0.92	0.90	0.92	0.91	0.95	0.91

themselves. In the control group, vertical stress at the block bottoms is unevenly distributed from the 3rd to the 11th block, indicating prolonged and dispersed stress exposure. With the Category II design, stress is concentrated mainly within blocks 9 ~ 11, reducing the extent of unevenness and potentially slowing damage accumulation within the asphalt blocks.

Category III aims to improve vibration characteristics. Here, acceleration distributions before and after optimization show only minor numerical differences, with slightly lower peak accelerations in the optimized case. This suggests that, for the current PEACT configuration, arrangement optimization has limited influence on vibration reduction, and the achievable improvements are modest compared to structural or material-focused optimizations.

To further illustrate the optimization effects, the maximum values of SL_U2, AB_D_S22, and S_A2 at various cross-sectional time intervals are compared for the three optimized schemes and the control group, as shown in Fig. 14. As seen in Fig. 14(a) and Fig. 14(b), the optimized schemes do not produce significant reductions in the absolute levels of dynamic response. This is expected, as rearranging the asphalt blocks does not alter their intrinsic material properties; under identical loading conditions, peak response magnitudes remain similar.

However, a clear benefit of the optimized arrangements lies in the smoothness of the longitudinal response variations. Compared with the control group, Categories I and II achieve markedly smoother changes. When fitting the longitudinal response variations using the method described in Section 3.1, the R^2 values for Categories I and II reach 0.842 and 0.901, respectively, substantially higher than the control group's 0.252 and 0.819 for the same cases. These results confirm that the optimized arrangements effectively promote continuous, gradual changes in dynamic response across the PEACT transition zone.

By contrast, the difference between Category III and the control group in terms of vertical acceleration is negligible, reinforcing the earlier finding that vibration-focused optimization has a limited impact under the present design constraints. Overall, for transition zone design, arrangement optimization should prioritize structural stress–strain performance. Between the two viable schemes, Category I is recommended as the final choice, as it not only improves response smoothness but also achieves continuous stiffness transitions along the track.

Finally, the three optimized design schemes are further evaluated using non-linear indicators as a robustness check. Although the opti-

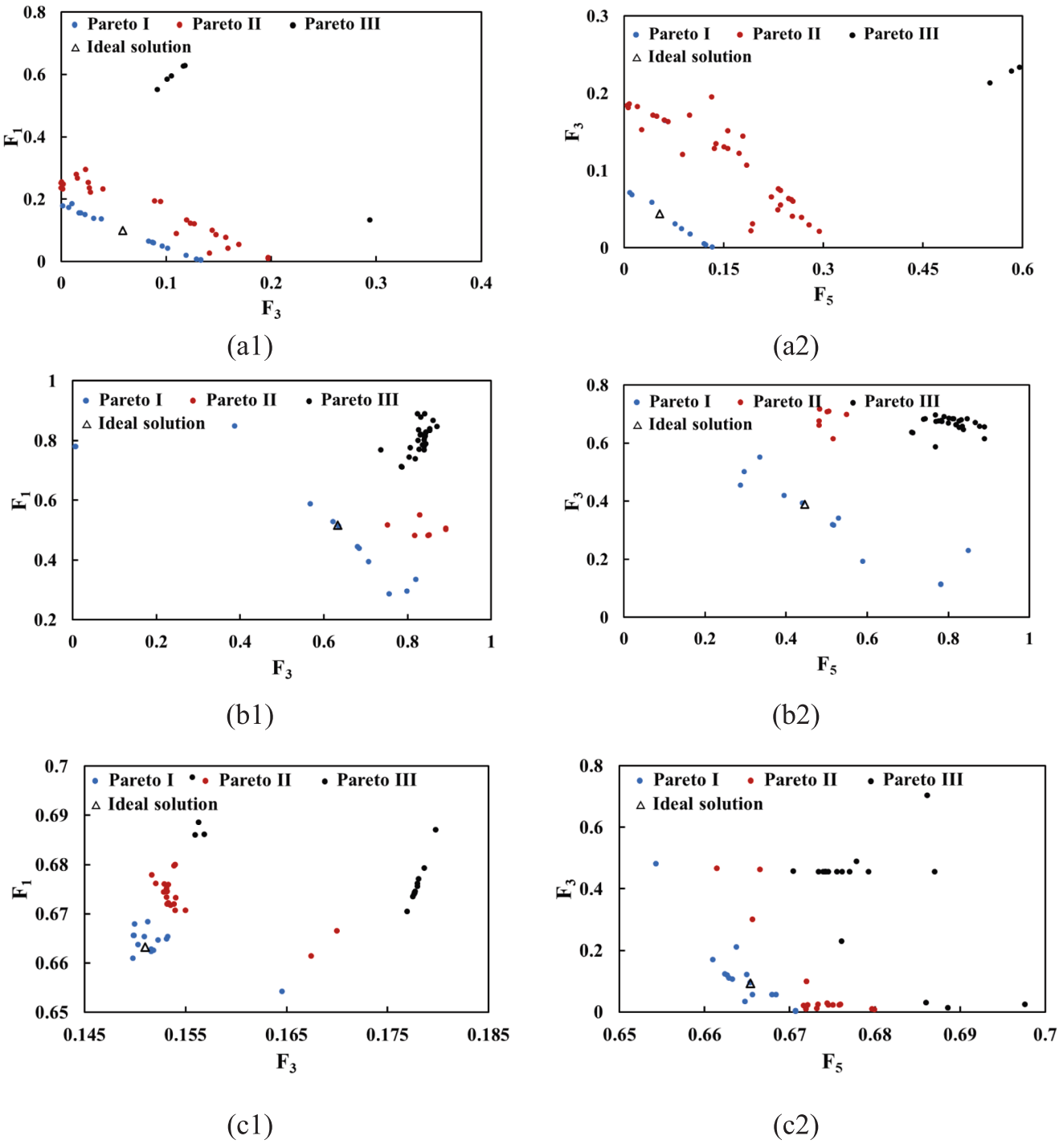

Fig. 11. Optimizing the arrangement method of PEACT, taking (a1) category I-F_1F_3, (a2) category I-F_3F_5, (b1) category II-F_1F_3, (b2) category II-F_3F_5, (c1) category III-F_1F_3, (c2) category III-F_3F_5 as examples.

Table 10
Optimized arrangement methods of asphalt block in PEACT.

Category	EA-6 CR (x_1)	EA-4 CR (x_2)	EA-2 CR (x_3)	EA-0 CR (x_4)	Sum
I	6	15	15	14	50
II	6	13	16	13	48
III	6	7	16	10	39

mization framework is formulated based on linear smoothness indicators, non-linear fitting methods are introduced here for post-hoc evaluation. Specifically, a third-order polynomial approximation is applied to the longitudinal distributions of representative response parameters shown in Fig. 14, and the corresponding coefficients of determination are calculated, as summarized in Table 11, in which R_1^2 and R_2^2 denote the goodness of fit obtained from linear and third-order polynomial fitting, respectively. The results show that, for all examined cases, the optimized schemes consistently exhibit higher smoothness levels than the control configuration under both linear and non-linear evaluations. More importantly, the relative ranking between

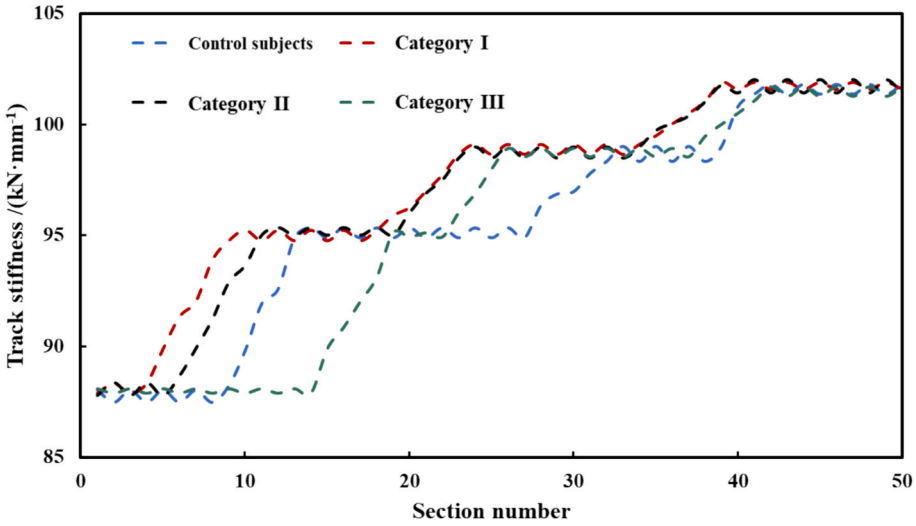

Fig. 12. Track stiffness under different arrangement methods.

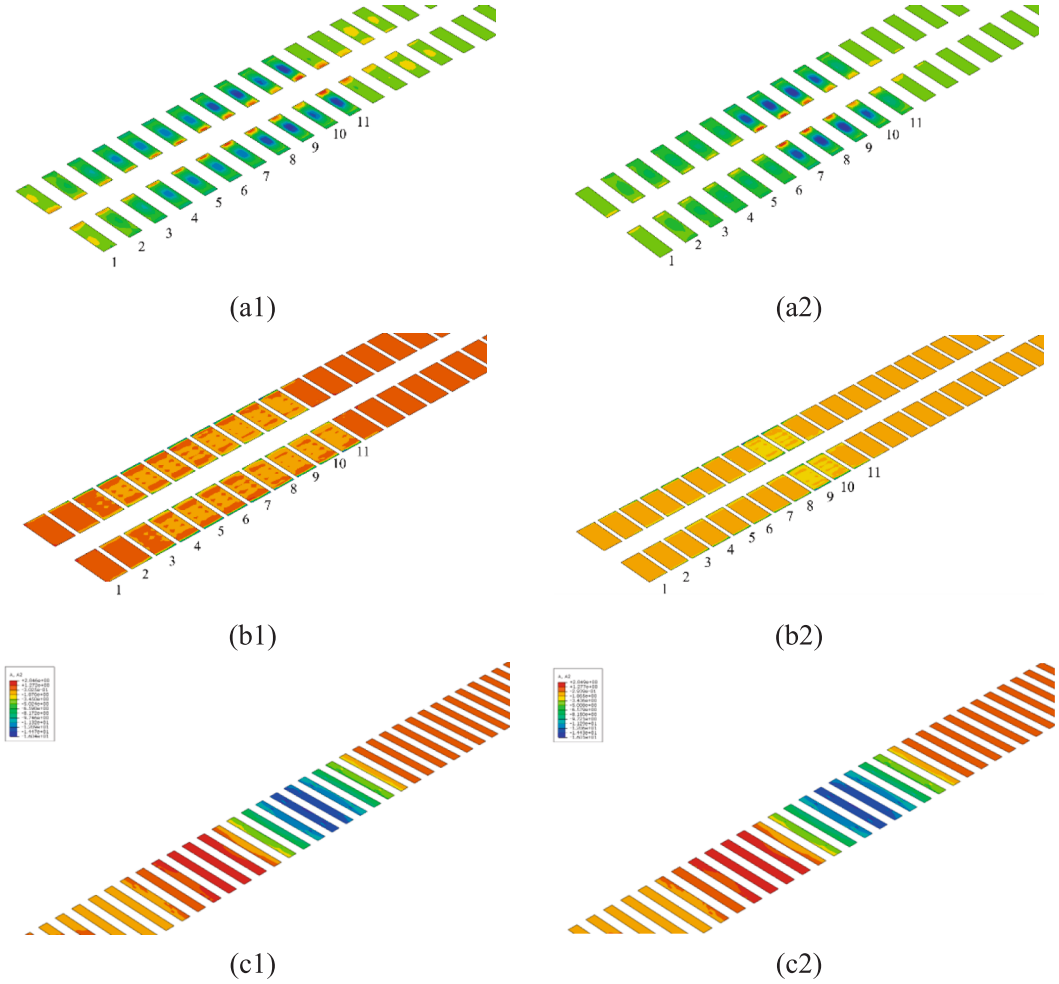

Fig. 13. Evaluation based on dynamic response (a) taking Category I and AB_T_U2 as an example, (b) taking Category II and AB_D_S22 as an example, and (c) taking Category III and S_A2 as an example (a1, b1, c1: control subject, a2, b2, c2: optimized category).

optimized and control schemes remains unchanged when non-linear indicators are adopted. This consistency confirms that the linear indicators used in the optimization process do not mislead the design decisions and are sufficient for identifying improved transition-zone layouts under the present modeling assumptions.

It is also noted that for vibration-related parameters such as S_A2, both linear and non-linear fitting yield low coefficients of determination for all schemes. This reflects the limited sensitivity of these parameters to DREAMs arrangement under the simplified moving-load excitation adopted in this study, as discussed earlier, and does not affect the overall

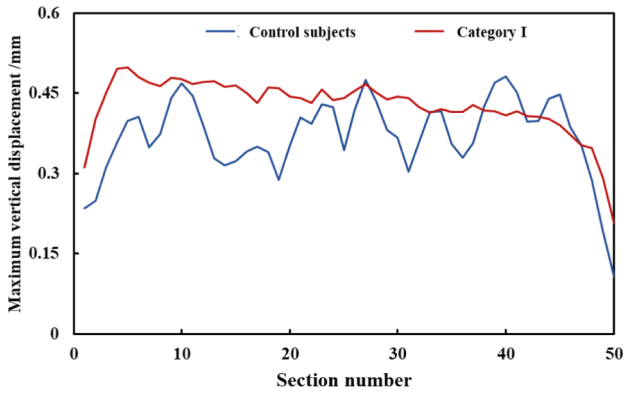

(a)

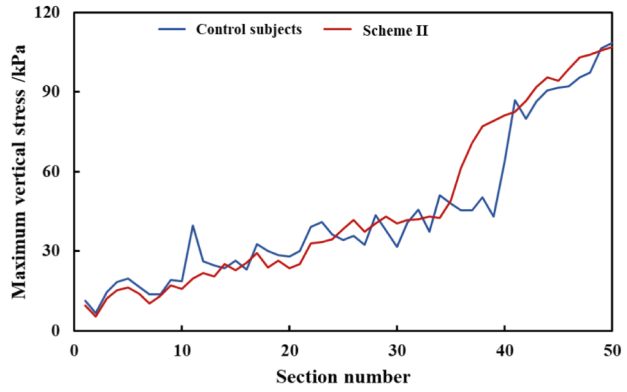

(b)

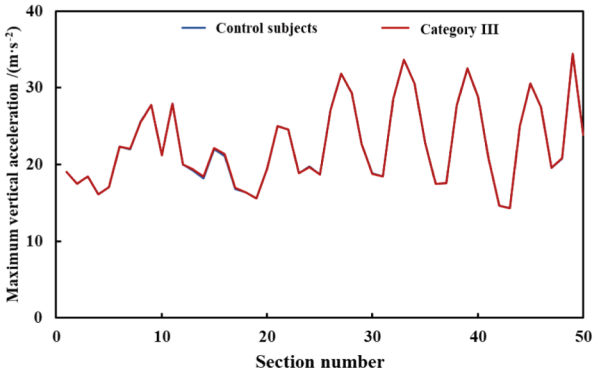

(c)

Fig. 14. Evaluation based on longitudinal distribution of track parameters, taking (a) category I and SL_U2, (b) category II and AB_D_S22, and (c) category III and S_A2, as examples.

Table 11
Comparison of linear and nonlinear smoothness indicators for the design schemes.

Parameter	Design scheme	R_1^2	R_2^2
SL_U2	Control subject	0.252	0.248
	Category I	0.842	0.654
AB_D_S22	Control subject	0.819	0.946
	Category II	0.901	0.974
S_A2	Control subject	0.104	0.108
	Category IIII	0.104	0.108

conclusions regarding layout optimization.

Conclusions

In this study, a performance-driven and data-assisted multi-objective optimization framework is proposed for designing railway transition zones, using the PEACT as an example. A validated 3D FE model is employed to generate a dataset of dynamic responses for multiple asphalt block arrangement schemes. The longitudinal variation of 13 selected dynamic response parameters is quantified with linear fitting indices (k and R^2). Subsequently, a series of NN-IIs is developed to predict the longitudinal variation of each dynamic response, and their training parameters are further optimized with NSGA-II to enhance accuracy. The NN-IIs are then integrated with NSGA-II to optimize the design scheme of the PEACT transition zone. The main findings can be summarized as follows:

- The number and arrangement of asphalt blocks have a limited influence on the peak values of dynamic responses in the transition zone. Still, they can markedly improve the smoothness of their longitudinal variation.
- Three optimized schemes were obtained, targeting: (i) structural working conditions (Category I), (ii) asphalt block working conditions (Category II), and (iii) vibration reduction (Category III).
- Both Category I and Category II schemes achieved substantial improvement in the smoothness of longitudinal dynamic responses compared with the control group (10–20-10–10), with the coefficient of determination R^2 increasing from 0.252 to 0.842 (Category I) and from 0.819 to 0.901 (Category II), respectively.
- Category I also improved the continuity of longitudinal stiffness distribution by reducing the frequency and extent of stiffness platforms and is therefore recommended as the most balanced design scheme for PEACT transition zones under the conditions considered in this study.
- Optimization based solely on vibration reduction (Category III) showed limited improvement, suggesting that vibration-related objectives may require additional design variables beyond asphalt block arrangement.

The proposed framework enables efficient exploration of the complex design space of transition zones without excessive FE computations, offering a transferable approach for other systems similar to the PEACT transition zone design. Future work will focus on refining the selection of dynamic response parameters to better align with railway engineering practices, incorporating wheel–rail interaction into the FE model to improve vibration prediction accuracy, and exploring alternative machine learning and optimization techniques better suited for small datasets.

CRediT authorship contribution statement

You Wu: Writing – review & editing, Writing – original draft, Visualization, Validation, Methodology, Investigation, Formal analysis, Data curation, Conceptualization. **Chenguang Shi:** Writing – review & editing, Writing – original draft, Methodology, Investigation, Funding acquisition, Conceptualization. **Yunhong Yu:** Writing – review & editing, Writing – original draft, Data curation, Conceptualization. **Yulou Fan:** Writing – review & editing, Writing – original draft. **Jun Yang:** Writing – review & editing, Supervision, Resources, Funding acquisition.

Declaration of competing interest

The authors declare that they have no known competing financial interests or personal relationships that could have appeared to influence the work reported in this paper.

Acknowledgment

The authors acknowledge the financial support of the National Natural Science Foundation of China (No. 52508484, No. 52078130, No. 52378444), the Natural Science Foundation of Chongqing (CSTB2025NSCQ-GPX0872), China Postdoctoral Science Foundation under Grant Number (2025MD774152).

Appendix

Algorithm of NSGA-II.

NSGA-II was first proposed by Deb et al. [40], an updated version of NSGA-I, which was introduced in 2002. NSGA-II introduces an elite strategy to address issues such as high computational complexity, loss of satisfactory solutions, and over-reliance on shared radii in the original NSGA. For example, the complexity of NSGA-II is $O(MN^2)$, and for NSGA, its complexity is $O(MN^3)$ [40]. The core of NSGA-II lies in sorting non-dominated solutions in the Pareto space through Pareto non-domination sorting and crowding degree comparison, ultimately yielding the optimal feasible solution set.

The multi-objective optimization problem can be described as

$$\min_{\boldsymbol{x}\in\Omega}\boldsymbol{F}(\boldsymbol{x}) = (f_1(\boldsymbol{x}), f_2(\boldsymbol{x}), \cdots, f_m(\boldsymbol{x}))\# \tag{A1}$$

where $\boldsymbol{x} = (x_1, x_2, \cdots, x_n)$ is the decision vector. $\Omega \subseteq \mathbb{R}^n$ is the feasible region. $f_k(x)$ represents the k th objective function.

The Pareto dominance is defined as follows:

A solution $\boldsymbol{x_a}$ dominates $\boldsymbol{x_b}$ ($\boldsymbol{x_a} \prec \boldsymbol{x_b}$) if

$$\forall i \in \{1, 2, \cdots, m\}, f_i(\boldsymbol{x_a}) \le f_i(\boldsymbol{x_b}) and \exists j, f_j(\boldsymbol{x_a}) < f_i(\boldsymbol{x_b})\# \tag{A2}$$

A solution is Pareto optimal if no other solution in Ω dominates it. The set of all Pareto optimal solutions forms the Pareto front, as shown in Fig. A.1(a). Fig. A.1(a) also exhibits the non-dominating sorting process. For each individual p, let n_p be the number of individuals dominating$p$

$$n_p = |\{q | q \prec p\}|\# \tag{A3}$$

let S_p be the set of individuals dominated by p

$$S_p = |\{q | p \prec q\}|\# \tag{A4}$$

If $n_p = 0$, p belongs to the first front F_1. Subsequent fronts F_2, F_3, … are identified iteratively.

For individuals within the same front F_k, crowding distance d_i measures the density of solutions around i to maintain diversity, as denoted in Fig. A.1(b).

$$d_i = \sum_{m=1}^{M} \frac{f_m(i+1) - f_m(i-1)}{f_m^{max} - f_m^{min}}\# \tag{A5}$$

where $f_m(i+1)$ and $f_m(i-1)$ are the neighboring solutions in the sorted list for the objective m.

Through non-dominated sorting and crowding distance calculation, all individuals in a given generation can be ranked according to their superiority or inferiority, and individuals for the next generation can be selected through an elite strategy.

Let P_t be the parent population and Q_t the offspring population. Merge

$$R_t = P_t \cup Q_t\# \tag{A6}$$

Perform non-dominated sorting to obtain fronts. F_1, F_2, …. Fill P_{t+1} from F_1 onward until reaching the population size N. If adding F_k exceeds N, select the most widely spaced solutions using crowding distance.

In this study, the above NSGA-II framework is applied to optimize the training parameters of NN-I, and design the scheme of PEACT transition zone, where the objective functions ($f_1, f_1, \ldots, f_m$) correspond to the accuracy and efficiency of NN-I, or k and R^2 Corresponding to the linear fitting equation of each dynamic response in each category, respectively. The optimization variables are the number of four types of DREAM blocks in the transition zone, as described in Sections 2.1, 3.2, and 4.2.

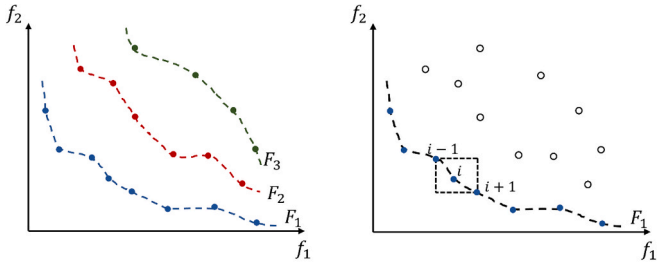

Fig. A1. Schematic of (a) non-dominated sorting, and (b) crowding distance calculation

Data availability

Data will be made available on request.

References

[1] Wang H, Markine V. Dynamic behaviour of the track in transitions zones considering the differential settlement. J Sound Vib 2019;459.
[2] Chen J, Chen R, Wang P, Xu J, An B, Yang F, et al. Wheel-Rail impact and vibration characteristic frequencies at High-speed railway turnouts. Mech Syst Sig Process 2024;218.
[3] Wang H, Markine V. Corrective countermeasure for track transition zones in railways: Adjustable fastener. Eng Struct 2018;169:1–14.
[4] Yu S, Shen S, Huang H, Zhang C. Engineered Semi-Flexible Composite Mixture Design and its Implementation Method at Railroad Bridge Approach. Transp Res Rec 2021;2675(9):789–97.
[5] Ramos A, Gomes Correia A, Calçada R, Connolly DP. Ballastless railway track transition zones: an embankment to tunnel analysis. Transp Geotech 2022;33:100728.
[6] Aggestam E, Nielsen JCO. Multi-objective optimisation of transition zones between slab track and ballasted track using a genetic algorithm. J Sound Vib 2019;446:91–112.
[7] D'Angelo G, Thom N, Lo Presti D. Bitumen stabilized ballast: a potential solution for railway track-bed. Constr Build Mater 2016;124:118–26.
[8] Wu Y, Shi C, Yu Y, Chen H, Fan Y, Wang H, et al. Dynamic behavior of precast epoxy asphalt track bed for transition zone in high-speed railway: a numerical approach. Transp Geotech 2023;40:100960.
[9] Shi C, Zhang H, Wang T, Zhou Y, Liu S, Wang H, et al. Design and performance evaluation of Bi-block precast rubberized epoxy asphalt trackbed for railway. Constr Build Mater 2021;313:125347.
[10] Shi C, Sun X, Wang T, Wu Y, Liu S, Wang H, et al. Numerical analysis of dynamic behavior of Bi-block precast asphalt trackbed for High-speed railway. Constr Build Mater 2022;342:128088.
[11] Wang T, Shi C, Yu Y, Xu G, Liu S, Wang H, et al. Mechanical properties evaluation of crumb rubber asphalt mixture for elastic trackbed. Constr Build Mater 2022;331.
[12] Wu Y, Zhou Y, Shi C, Yu Y, Fan Y, Cai X, et al. Interlayer bonding quality evaluation of sleeper-asphalt block composite structure applied to asphalt elastic cured track bed. Constr Build Mater 2024;415.
[13] Shi C, Wu Y, Fu C, Yang J. Mechanical properties of rubberized epoxy asphalt mixture used in railway infrastructure, advances in Functional Pavements. CRC Press 2024:22–6.
[14] Shi C, Wu Y, Fuentes R, Fan Y, Zhou Y, Fu C, et al. Volumetric mix-design modification and vibration attenuation analysis of rubberised epoxy asphalt track for railway. Road Mater Pavement Des 2024:1–24.
[15] Li J, Shang M, Liu G, Yang T, Pan Y, Zhou J, et al. Two-step improvements of volumetric design method based on multi-point supported skeleton for asphalt mixtures. Constr Build Mater 2019;217:456–72.
[16] Li J, Shang M, Pan Y, Liu G, Chen A, Zhou J, et al. Laboratory improvement and field assessment of Volumetric design method based on multi-point Supported skeleton for asphalt mixtures [VS method]. Constr Build Mater 2019;224:962–79.
[17] Zu-yuan L, Hou-zhi W, Chen-guang S, Xing C, Jun Y, Yun-hong Y. Evaluation of the fractures of asphalt concrete added with rubber particles based on the fine aggregate mixtures. Constr Build Mater 2022;332.
[18] Kennedy J, Woodward PK, Medero G, Banimahd M. Reducing railway track settlement using three-dimensional polyurethane polymer reinforcement of the ballast. Constr Build Mater 2013;44:615–25.
[19] Woodward PK, Kennedy J, Laghrouche O, Connolly DP, Medero G. Study of railway track stiffness modification by polyurethane reinforcement of the ballast. Transp Geotech 2014;1(4):214–24.
[20] Jing G, Qie L, Markine V, Jia W. Polyurethane reinforced ballasted track: Review, innovation and challenge. Constr Build Mater 2019;208:734–48.
[21] Xiao X, Wang J, Cai D, Lou L, Xiao F. A novel application of thermoplastic polyurethane/waste rubber powder blend for waterproof seal layer in high-speed railway. Transp Geotech 2021;27.
[22] Yonggang W. Optimal Design Scheme of Prefabricated polyurethane Curing Track Bed. Railway Standard Design 2022;66(11):58–62.
[23] Shen C, Zhang P, Dollevoet R, Zoeteman A, Li Z. Evaluating railway track stiffness using axle box accelerations: a digital twin approach. Mech Syst Sig Process 2023;204.
[24] Shen C, Dollevoet R, Li Z. Fast and robust identification of railway track stiffness from simple field measurement. Mech Syst Sig Process 2021;152.
[25] Jain A, Marykovskiy Y, Metrikine AV, van Dalen KN. Quantifying the impact of stiffness distributions on the dynamic behaviour of railway transition zones. Transp Geotech 2024;45.
[26] Lv W. Structural analysis and design method for sub-grade Bed of heavy haul railway, 1) MOE Key Laboratory of High-speed Railway Engineering, Southwest Jiaotong University, Chengdu; 610031, China (2) China Railway Siyuan Survey and Design Group Co, Ltd, Wuhan; 430063, China (3) Institute of Architec 2016;38(4):74–80.
[27] Liu S, Chen X, Ma Y, Yang J, Cai D, Yang G. Modelling and in-situ measurement of dynamic behavior of asphalt supporting layer in slab track system. Constr Build Mater 2019;228.
[28] Williams ML, Landel RF, Ferry JD. The temperature dependence of relaxation mechanisms in amorphous polymers and other glass-forming liquids. J Am Chem Soc 1955;77(14):3701–7.
[29] ABAQUS Analysis User's Manual. Time domain viscoelasticity. https://classes.engineering.wustl.edu/2009/spring/mase5513/abaqus/docs/v6.6/books/usb/default.htm?startat=pt05ch17s07abm11.html.
[30] Shih J-Y, Thompson D, Zervos A. The effect of boundary conditions, model size and damping models in the finite element modelling of a moving load on a track/ground system. Soil Dyn Earthq Eng 2016;89:12–27.
[31] Shi C, Wu Y, Wang T, Yu Y, Wang H, Yang J. Rheological properties and polymer phase structure characterization of SBS/CR composite modified asphalt (CMA) binders. Mater Struct 2023;56(2):33.
[32] Chen H, Trivedi AR, Siviour CR. Application of Linear Viscoelastic Continuum damage Theory to the Low and High Strain Rate Response of Thermoplastic polyurethane. Exp Mech 2020;60(7):925–36.
[33] L. China Railway Siyuan Survey and Design Group Co., Code for Design of Railway Track, 2018.
[34] Park Y-S, Kim S, Kim N, Lee J-J. Finite element model updating considering boundary conditions using neural networks. Eng Struct 2017;150:511–9.
[35] Standard Test Methods of Asphalt and Asphalt Mixture for Highway Engineering, Ministry of Transport of the People's Republic of China, 2025.
[36] Jiang H, Bian X, Cheng C, Chen Y, Chen R. Simulating train moving loads in physical model testing of railway infrastructure and its numerical calibration. Acta Geotech 2014;11(2):231–42.
[37] Liu Y, Qian Z-D, Zheng D, Huang Q-B. Evaluation of epoxy asphalt-based concrete substructure for high-speed railway ballastless track. Constr Build Mater 2018;162:229–38.
[38] Jiang H, Li X, Xin G, Yao Z, Zhang J, Liang M. Geometry mapping and additional stresses of ballastless track structure caused by subgrade differential settlement under self-weight loads in high-speed railways. Transp Geotech 2019;18:103–10.
[39] Gunantara N. A review of multi-objective optimization: Methods and its applications. Cogent Eng 2018;5(1):1502242.
[40] Deb K, Pratap A, Agarwal S, Meyarivan T. A fast and elitist multiobjective genetic algorithm: NSGA-II. IEEE Trans Evol Comput 2002;6(2):182–97.